Five kHz Thermometry in Turbulent Spray Flames using Chirped-Probe Pulse Femtosecond CARS, Part I: Processing and Interference Analysis

Levi M. Thomas,[1,*] Albyn Lowe,[2] Aman Satija,[1] Assaad R. Masri,[2] and Robert P. Lucht[1]

[1]School of Mechanical Engineering, Purdue University, West Lafayette, IN 47906 USA
[2]School of Aerospace Mechanical and Mechatronic Engineering, University of Sydney, NSW 2006, Australia
*Corresponding author: Levi.13.Thomas@gmail.com

Abstract:
We have applied chirped-probe-pulse (CPP) femtosecond (fs) coherent anti-Stokes Raman scattering for 5 kHz temperature measurements in turbulent spray flames. The CPP fs CARS technique has previously been used to perform spectroscopic temperature measurements in highly turbulent laboratory burners with excellent accuracy, precision, temporal resolution, and spatial resolution. In this paper, ultrafast CARS measurements in spray flames are presented as part of a larger effort to provide spatially and temporally resolved temperature fields in harsh spray environments. The Sydney Needle Spray Burner (SYNSBURN^{TM}) was used to stabilize turbulent spray flames of acetone and ethanol. The burner features a retractable fuel injector so that the droplet density at the nozzle exit could be systematically varied. Results from selected regions of the turbulent spray flames are discussed in detail to highlight the challenges of CPP fs CARS temperature measurements. Sources of spectral distortion due to interaction with droplets are discussed along with an uncertainty analysis. The passage of fuel through the probe volume caused varying levels of signal degradation and resulted in complete signal loss on approximately 10% of the laser shots for dense spray conditions. The interferences are attributed to two separate phenomena and are categorized based on the probable phase of the fuel – liquid or gas. Interference caused by liquid fuel was unavoidable in certain regions at certain operating conditions, but easily identified and removed. Interference from vapor fuel was more problematic as the nitrogen signal was only moderately corrupted in the high-frequency portion of the spectrum, and the temperature was generally biased to higher values. Rejecting individual signal spectra, based on a fitting error threshold, was shown to be effective in excluding shots with significant interference from fuel droplets, but shots with only minor interference require a more-advanced rejection criterion. Analysis of the temperature fields for a few selected conditions is presented showing trends with the atomization quality of the liquid fuel. Fourier analysis revealed hydrodynamic instabilities in the shear layer and relatively weak thermoacoustic instabilities in the reaction zone.

Keywords: Laser diagnostics, Coherent anti-Stokes Raman scattering, Ultrafast spectroscopy, spray flames, Turbulent combustion

1. Introduction

Spray combustors are ubiquitous in practical applications yet the underlying physics involved in the atomization, combustion and pollutant formation stages is not well-understood. This necessitates additional measurements to advance such understanding and to enable the optimization of combustor designs for gas-turbine engines [1] and for internal combustion engines [2,3]. Laser diagnostic approaches are non-intrusive, precise, and exhibit excellent spatial and temporal resolution [4]. However, the turbid environment of two-phase combustion is inherently more challenging for laser diagnostic techniques than gaseous flows; this is primarily due to scatter and absorption. Some of the successful approaches in studying two-phase combustion thus far are phase-Doppler anemometry [5], combined phase-Doppler interferometry and planar laser-induced fluorescence [6], digital inline holography [7], high-speed microscopic shadowgraphy [8], and Raman scattering [9].

Temperature is one of the most important state quantities used, in conjunction with other parameters to determine the burning as well as emission characteristics of practical systems [10]. Coherent anti-Stokes Raman scattering (CARS) spectroscopy is often used for combustion temperature measurements in highly-luminous [11,12] and/or particle-laden flames, as it yields arguably the best combination of strong signal levels, accuracy, precision, and excellent temporal resolution [13]. Recent advances in commercially available, ultrafast laser technology have enabled CARS experiments to move from the nanosecond [14] to the femtosecond timescale [15]. The kHz-scale pulse repetition frequency and femtosecond/picosecond timescales employed with ultrafast CARS techniques are beneficial in investigating the highly-turbulent combustion environment of swirl burners [16,17], and the dynamics between heat release and turbulence [18,19]. Relatively few thermometry studies have been published using CARS in reacting spray environments. Two notable exceptions, both from the University of Erlangen-Nuremberg, were from Beyrau et al. [20] in the vaporizing spray of a gasoline fuel injector in 2004, and Engel et al. [21] in the liquid and particle regime of a spray pyrolysis process in 2012. Both studies, which used pure rotational nanosecond CARS, suffered significant signal dropout in the turbid combustion environments.

The application of chirped-probe pulse femtosecond coherent anti-Stokes Raman scattering (CPP fs CARS) spectroscopy in turbulent spray flames is discussed in this paper, and temporally-

resolved temperature measurements from selected regions and operating conditions are presented to illustrate the diagnostic challenges in probing such flows. The CPP fs CARS measurements are part of a larger study aimed at providing detailed and novel mapping of temperature fields in spray flames ranging from dilute to dense [22]; issues associated with the application of CPP fs CARS in spray flames and the discussion of the accuracy and precision of the results are discussed in much more detail in this paper while the *part 2 paper* [23] focuses on the structure of the reaction zones. The Sydney Needle Spray Burner (SYNSBURN^{TM}) serves as a platform for technique validation and demonstrates the potential capability of CPP fs CARS in more complex multi-phase applications. The burner is designed to generate well-characterized flames with spray flows that can span a range of spray loadings and turbulence levels for insight into physical phenomena including atomization, multi-phase mixing, and turbulent combustion. Given the well-defined boundary conditions, the burner is ideally suited for the validation of computational models. Detailed datasets of flow field characteristics have been extensively studied previously in [8] and temperature measurements will complement this existing dataset.

Section 2 of the paper provides details on the CPP fs CARS technique and the data processing methodology along with a brief description of the burner and the selected cases. Section 3 reports issues regarding signal interference, errors and corrections. The final section of the paper reports time series analysis and samples of temperature statistics. This forms a relevant lead-up to subsequent publications [23] where detailed statistics about the flame structure are presented.

2. Experimental System

This section describes the optical setup for the CPP fs CARS system and the spectral fitting methodology employed to extract temperature for the spray flame dataset. The specific details about technique development and performance for CPP fs CARS are published in [24]. Here we focus on distinct interferences found in spray flames and methods to ensure the validity of the results. A brief description of the burner and the selected cases are included.

2.1. Signal Generation

The temperature sensitivity of CPP fs CARS comes from measuring the temporal decay of the macroscopic polarization of N_2 molecules in a phenomenon called frequency-spread dephasing (FSD). The polarization is generated when the pump and Stokes pulses interact simultaneously at the probe volume and a giant Raman coherence is generated. Initially, the coherences for each of the different Raman transitions, primarily Q-branch transitions, are in phase due to the impulsive pump-Stokes excitation. After the pump-Stokes excitation, the coherences for the different Q-branch resonances each begin to oscillate at their own characteristic transition frequency. Because these transition frequencies are different, the resonances begin to oscillate out of phase with each other and the initial giant Raman coherence decays, this is referred to as FSD. The FSD decay is an effective thermometer because the FSD rate is a strong function of temperature. Furthermore, the FSD is completely independent of collisional effects during the initial few picoseconds after excitation at atmospheric pressure [25]. The temporal behavior of the FSD is measured with the use of a frequency-chirped probe pulse (CPP) [26, 27]. When the probe beam scatters from the Raman coherence and generates the signal beam, the temporal decay of the Raman coherence is mapped onto the frequency content of the CPP fs CARS signal, and the FSD behavior is captured in the signal spectrum. This is not a direct mapping because of the influence of the nonresonant background and the temporal and frequency structure of the probe beam must also be taken into account. This time-to-frequency mapping of the FSD in the signal beam is the primary mechanism in CPP fs CARS thermometry. A detailed description of the fs CARS process is available in published literature [26, 28].

2.2. Ultrafast Laser System

Seed pulses from a mode-locked Titanium:Sapphire (Ti:S) oscillator are amplified from 5 nJ up to 2.0 mJ via chirped-pulse amplification in four stages: a stretcher, a Ti:S regenerative amplifier, a single-pass Ti:S amplifier, and a compressor. The two Ti:S amplifier stages are optically pumped with approximately 7 mJ/pulse each from the frequency-doubled output from an Nd:YLF laser. At the amplifier exit, each pulse has 2 mJ of energy and approximately 60-fs temporal duration (FWHM). Six percent of this energy is used directly as the pump beam, while 14% is sent through a 30-cm long SF-10 glass rod to create the chirped probe pulse (CPP). The remaining 80% of the 2-mJ pulse energy is used to pump an optical parametric amplifier and generate the

Stokes pulse centered on 982 nm. The optical parametric amplifier (OPA) is tuned such that the pump-Stokes frequency difference excites Q-branch vibrational transitions ($\Delta v=+1$, $\Delta J=0$) around 2,330 cm^{-1}. The OPA is configured to use the frequency-doubled idler beam instead of the frequency-doubled signal beam that was used in an earlier turbulent flame investigation [18]. The pulse energy of the frequency-doubled idler beam was a factor of three less than the pulse energy of the frequency-doubled signal beams, but by using the 982-nm frequency-doubled idler beam as the Stokes beam we were able to use the fundamental 800-nm beam from the Ti:S amplifier for both the pump and probe beams. The resulting CARS signal was generated near 675 nm. The CARS signal frequency was shifted from the frequency of all the input laser beams. Scatter from the three CARS input beams was, therefore, effectively filtered out in the spectrometer.

2.3. CPP fs CARS System

As shown in Fig. 1, the three CARS beams are routed through time-of-flight delay stages to control timing overlap at the probe volume and through half waveplates to align polarizations. The folded-BOXCAR alignment geometry is used for phase-matching with a 90° folding angle for maximum spatial separation of the CARS signal from the input beams. A 250-mm, broadband-AR-coated, plano-convex (PCX) lens is used to focus the three beams.

A diamond pinhole aperture and birefringent crystal at the probe volume are used to find spatial and temporal overlap of the three beams. For spatial resolution, the diameter of the probe volume is estimated to be the waist of the most weakly-focusing beam, and the length is estimated by measuring the non-resonant signal generated in a non-linear crystal translated through the probe volume. This spatial-resolution assessment of 60 x 790 μm (10% intensity to 10% intensity) is considered conservative in both dimensions, as neither the crossing angles of the CARS beams nor the crystal thickness of 100 μm were considered.

The three CARS input beams are blocked after interacting in the probe volume, and the signal is collimated with a 300-mm plano-convex lens and dispersed horizontally through a 0.5-m spectrometer onto the bottom 32 rows of a 1024 x 1024-pixel, electron-multiplying, charge-coupled device (EMCCD) camera (*iXon 888, Andor Technologies*). The camera is externally triggered and operated in full-vertical binning mode allowing for data acquisition at the laser

pulse repetition frequency (PRF) of 5 kHz. The back-illuminated EMCCD has a quantum efficiency of 87% at the center wavelength of the signal, 675 nm. For the data discussed in this paper, the EMCCD gain was not used (gain setting was set to unity).

2.4. Spectral Fitting

A detailed description of the original version of the spectral fitting code used in this work was published by Richardson, et al [29] in 2011; only a brief outline is given here. First, laser parameters are determined by comparing synthetically-generated spectra with a time-averaged spectrum obtained at a known temperature. This temperature calibration is performed at room temperature, and then across the range of flame temperatures in a nearly-adiabatic hydrogen-air flame stabilized over a Hencken burner. Laser parameters are considered to be converged once the squared error between the synthetically generated and the experimentally measured spectra is minimized. These laser parameters are then fixed and applied in fitting experimental spectra recorded during the following two to three hours. During the single-laser-shot fitting of these experimental spectra, the floating variables are the temperature, the ratio of resonant to non-resonant molecular response, and incremental vertical and horizontal shifts allowing for small deviations in frequency and signal strength. Five sets of laser parameters from room temperature and the four Hencken burner flames were used in the single-shot temperature determination. For each single shot spectrum all five sets of laser parameters are used to fit the spectrum and a fitting error is calculated. A new approach using weighting factors is then used to calculate the temperature, with the lowest error results being weighted the most [24]. For the spray flame experiments, 2,000 CARS spectra were acquired at each measurement location, resulting in 400-ms-long temperature histories. At select locations, however, 20,000 shots were recorded to assess long-term stability, ensure converged temperature statistics, and achieve the proper spectral resolution to identify coherent temperature structures when Fourier analysis is applied.

2.5. Calibration and Temperature Measurement Performance

As described in the previous section, a nearly-adiabatic hydrogen-air flame stabilized over a Hencken burner was used for temperature calibration at equivalence ratios ranging from $\phi = 0.3$ – 0.9 corresponding to adiabatic equilibrium temperatures ranging from 1187 – 2295 K. The

temperature measurement performance was characterized using a random testing procedure described in [24], where signal spectra acquired at known conditions were randomly selected and fit using the same procedure used to fit experimental data.

The individual results from each performance assessment performed during CPP fs CARS data acquisition in spray flames is shown in Fig. 2. Each of the data points in Fig. 2 represents the results of analyzing 2,300 single-laser shot CPP fs CARS spectra acquired from either room air or the Hencken burner.

Table 1 lists the averages of these results. Accuracy is defined as the difference between the average and adiabatic flame temperatures while precision is defined as the standard deviation of single-shot measurements; both are normalized by the local mean temperature.

$$Accuracy\ Error\ =\ (\bar{T} - T_{ad})/\bar{T} \tag{1}$$

$$Precision = \sigma/\bar{T} \tag{2}$$

In Table 1, the column labeled “Accuracy (abs.)” is the average of the absolute value of the mean temperature errors shown in Fig. 2. The column labeled “Avg. Accuracy (Mean Temp. Bias)” average of the value of the mean temperature errors shown in Fig. 2. The is second value is listed simply to show that there is no systematic bias in the determination of mean temperature, except near 300 K where the measured values tend to be about 8% (25 K) too high. For the 68 data sets recorded in the Hencken burner, the systematic errors in the mean temperature were 7% or less, except for two data points in the ϕ=0.3 flame. We can therefore regard ±7% as an upper limit systematic uncertainty in the temperature measurements at temperatures above 1,000 K.

This assessment of temperature-measurement performance is valid as long as the experimental environment is similar to the calibration environment in the Hencken burner flame. These assumptions may not be valid, for example, if a large proportion of the nitrogen probe gas was displaced with another substance, such as the vapor plume around a liquid fuel droplet, or if the spray fuel droplet itself were to pass through the probe volume. Spectral interference due to hydrocarbons in the probe volume was observed and will be discussed in Section 3.

2.6. Burner Characteristics and Selected Cases

The Sydney Needle Spray Burner (SYNSBURN^{TM}) is the focus of this investigative study on turbulent spray combustion [8]. This piloted burner was developed by the Clean Combustion Group at the University of Sydney and was installed into a co-flowing wind tunnel in the Applied Laser Spectroscopy Laboratory at Purdue University. The burner enables versatile control of inlet conditions and uses co-axial airblast atomization of a liquid jet issuing from a needle, to generate sprays ranging the full suite from dilute to dense. This novel aspect is possible by varying the recess length (Lr) of the needle tip within the airblast inner tube relative to the burner orifice. This allows direct control of the fuel residence time independent of the global Weber number or the bulk jet Reynolds number.

The spray reaction zone is anchored close to the burner surface by a coaxial piloted flame composed of premixed acetylene C_2H_2, hydrogen H_2, and air [30]. The pilot gas composition is set to match the carbon-to-hydrogen ratio of two selected liquid fuels, namely acetone (C/H=1/2) and ethanol (C/H=1/3). This results in pilot adiabatic flame temperatures of 2,493 K and 2,512 K for ethanol and acetone respectively. Acetone, C_3H_6O, and ethanol, C_2H_6O, are comparable due to their similar heating values and densities. Acetone, however, has a much higher volatility. The spray flame cases investigated here have been previously characterized in terms of their respective flow-fields and droplet size profiles using phase Doppler anemometry and laser Doppler velocimetry (PDA/LDV). High speed 10kHz microscopic backlit imaging has also been used to generate population distributions of liquid fragments using a novel classification scheme based on shape, and this is used to correlate the near and far-field structure of turbulent spray flames [8]. The naming methodology shown in Table 2 is consistent among these related publications and is demonstrated with reference to cases N-AF2-80 and N-EF8-25: N = Needle, A = Acetone or E=Ethanol, F refers to flames followed by a reference number defining flowrates setting and finally Lr = 80mm or 25 mm respectively. Here, the exit Weber number is defined as $We=\rho_g U_g^2 D_l/\sigma$ where ρ_g is the gas density, U_g is the bulk gas velocity, D_l is the diameter of the liquid fuel delivery, and σ is the surface tension. The fuel to air ratio (F/A) is defined as the mass fraction of injected liquid over that of the blast air; and Re_g and Re_l refer to the Reynolds numbers of the carrier air and liquid streams, respectively.

For every flame case studied, six radial scans at downstream locations x/D=0.3, 1, 3, 5, 10, 20 were collected to sufficiently resolve the temperature distribution across the entire spray flame front; this typically resulted in up to 126 probe volume locations at which a minimum of 2,300 single-laser-shot CARS spectra were recorded. The test matrix illustrated in Table 2 shows the magnitude of the dataset to be studied, involving acetone and ethanol fuels and recess lengths ranging 0, 10, 25, 40 and 80 mm for the four selected cases 2-8.

3. Interference Analysis: Influence of Fuel Spray on Gas-phase CARS Measurements

Analysis and temperature fitting of a CPP fs CARS spectrum assumes the signal is generated in nitrogen by three laser pulses of known specification. The presence of other substances, such as liquid fuel droplets, in the probe volume can interfere with the resonant CARS process in nitrogen. This section details the possible errors and interferences encountered in spray flames that influence the signal and hence the accuracy of the measured temperature.

The presence of a fuel spray influenced the CPP fs CARS signal in three primary ways: first, nitrogen gas was displaced from the probe volume decreasing the pure signal; second, resonant signals from other gas-phase hydrocarbons were generated in the probe volume; and third, liquid fuel droplets in the probe volume interacted with the focused input laser pulses. The first mechanism is the simplest; as the resonant species is displaced from the probe volume, less signal is generated. The CARS signal is proportional to the squared number density of the resonant species, and the signal-to-noise ratio decreases when nitrogen is displaced from the probe volume. The second mechanism proposes that gas-phase hydrocarbons in the probe volume can be excited by the wings of the broadband pump and Stokes pulses and contribute to the nitrogen signal. The third mechanism manifests when a liquid droplet passes through the probe volume just as the pump, Stokes, and probe laser pulses focus. When focused into a liquid-phase medium, the intense pulses undergo self-phase modulation and generate superfluorescence. The newly-generated light covers a range of frequencies resulting in broadband noise that spectrally overlaps the resonant nitrogen signal.

These three interference mechanisms affect the temperature measurement performance of the CPP fs CARS technique differently. Liquid droplets generate the strongest interference, and the spectra where liquid droplets interfere have such large fitting errors that the data from these

shots is discarded. Significant deviations to the signal spectrum result in large fitting error and are flagged in post-processing for removal. Such interference does result in data loss but does not significantly impact the results overall as these shots are easily identified and removed. This will bias the determination of mean temperature to some extent. In general, for regions where large numbers of droplets are present, rejecting these spectra will result in measured mean temperatures that are higher than the true mean temperature. Conversely, gas-phase fuel in the probe volume creates weaker signal interference but is more difficult to positively identify as interference. Relatively minor deviations, such as those seen in panel (c) of Fig. 5, actually present a more significant challenge as they are more difficult to identify as outliers compared to those seen in panel (b). With only small deviations due to gas-phase hydrocarbons in the probe volume, the spectral fitting code can compensate for the increased signal level in the high-frequency region of the signal spectrum by erroneously predicting a higher temperature.

Specific examples of signal interference are shown in Fig. 5 for two spray densities and two axial positions on the centerline where the spray is most dense. Each panel shows a 10-shot sequence overlay of raw CARS spectra during an interference event; 10 consecutive shots were sufficient to see an interference develop, peak, and vanish. Panel (a) shows the background acquired with the Stokes beam blocked, which typically results in no signal.

The background is typically recorded as a reference but exhibits erratic noise in the core of the denser sprays. The broad, smooth shape of the spectra recorded with the Stokes beam blocked, along with the rainbow-colored scatter visually observed with the probe volume at these locations, indicates superfluorescence, ionization, or other non-linear phenomena occurring in the fuel.

The strong spikes on the right sides of the CARS spectra showing interference are attributed to various C-H stretches in the fuel being excited off-resonance. Indeed, Raman spectroscopy shows peaks at 2,921 cm^{-1} for acetone and a group of three peaks at 2,878, 2,927, and 2,973 cm^{-1} for ethanol [31]. In a previous experiment with the same laser system, we were able to excite the symmetric stretch, ν_1, vibrational mode in methane at 2,913 cm^{-1} which is detuned nearly 600 cm^{-1} off-resonance, due to the broad bandwidth of CARS input pulses. In these experiments (see Fig. 6) the ro-vibrational CARS signal from methane exhibited a similar shape and occurred

at the same spectral location as the interference spikes observed on the low wavelength (right) side of some of the subplots in Fig. 5. The time-averaged CPP fs CARS spectrum of the binary N_2-CH_4 mixture, shown in Fig. 6, illustrates the influence on the nitrogen signal when significant levels of hydrocarbons are present in the probe volume.

The grating angle in the spectrometer was adjusted to directly view the CH_4 signal contribution, but the CARS beams were not detuned from the nitrogen resonance at 2,330 cm^{-1}. For reference, spectra were acquired in pure CH_4 with the CARS system tuned to excite the ν_1 vibrational mode in methane at 2,913 cm^{-1}. The pure methane signal peaks near 15,400 cm^{-1}., which matches the anti-Stokes frequency shift from the probe center of 12,500 cm^{-1} (800 nm). The spectral location and shape of the interferences encountered in the spray flames compared to the measurements in the gas cell offer strong evidence the interference originated from C-H vibrational resonances in the hydrocarbon fuel. Likewise, the broadband fluctuations in the noise floor shown in panel (a) of Fig. 5 supports the separate signal interference mechanism proposed that liquid droplets interact with the focused laser pulses in a fundamentally different way.

The average squared fitting error for each shot is used to discriminate laser shots with significant distortion. This value is determined as the sum of the squared difference between the experimental spectrum and the synthetic “best fit” spectrum divided by the number of points considered in the spectral region of interest. It represents the average fit error per camera pixel over the actual CARS signal spectrum. Since the spectral fitting model accounts for only the signal from nitrogen, abnormally large fitting errors are generated during shots with spectral interference. During validation testing with a premixed methane-air jet flame, the average fitting error was generally less than 1.0% over a range of flame temperatures. A threshold for fitting error was therefore chosen at 2.0% and this was employed in processing the spray flame spectra while monitoring the residual fitting error versus temperature profile. In the absence of interferences, this threshold of 2.0% for the fitting error profile is adequate to ensure correspondence between the CARS signal levels and temperature in atmospheric-pressure flames.

Figure 7 shows the extent of the shot rejection due to the application of this 2% threshold at various axial and radial locations in case N-AF2-40. Also shown in Fig. 7 are profiles of average fitting error which are all below the 2% threshold. It is evident from the radial profiles that the total shot rejection rate is most severe on centerline and close to the exit plane. Directly over the liquid fuel needle, the rejection rate was as high as 78% for the flame case with highest fuel loading. This profile of shot rejection reduces with radial distance and height above the burner as the droplets dispersed such that the shot rejection rate averaged over the entire radial scan fell from 15% to around 10%.

The fitting error shown on the right ordinate of each panel in Fig. 7 shows the average error after rejecting shots with bad fits. These error profiles show only minor covariance with the shot-rejection profiles indicating that shots with bad fits are effectively excluded by the error threshold. While no temperature data is available for the rejected shots, the ability to distinguish between uncorrupted CARS spectra, those with interferences from gas-phase hydrocarbons, and those with interferences from liquid-phase hydrocarbons may provide a diagnostic of the evaporation characteristics in spray flames for future analysis.

4. Sample Results

This section reports sample temperature time series at various locations within acetone spray flames with accompanying statistics and analysis. Trends in the average temperature fields and in the temperature spectra are shown with respect to fuel spray density.

4.1. Point Temperature Measurements at 5 kHz

Fig. *8* panel (**a**) shows 400 ms temperature histories at x/D=1 across r/D=0.8-1.6 and b) is a "magnified view" of 50 ms of the same data for clarity. At the expanded time scale, individual temperature values are visible and temperature fluctuations are well resolved in the lower-temperature region outside the flame zone.

The trace from r/D = 0.8 in panel (**b**) of Fig. 8 displays the temperature history near the pilot flame where the temperature is expected to be relatively steady and slightly below the adiabatic flame temperature for the 3-gas pilot of 2,512 K. The average temperature and RMS fluctuation values were 2,396 K and ±116 K (4.8%). The RMS fluctuation level at this point is only

moderately higher than the system precision near this temperature, measured to be 3.4% in the calibration flame at 2,295 K. The first peak in the power spectral density occurs at 59 Hz and is ~10^{-4} weaker than the constant temperature component. Signal drop-out away from centerline is less significant due to the extremely small probe volume and the scarcity of droplets away from the centerline. No drop-outs were observed in the temperature histories at the probe-volume locations shown in Fig. 8.

In terms of turbulence statistics, the mean temperature converges in about 10 ms (50 laser shots) and its rms fluctuation typically converges after 40-50 ms (200-250 laser shots) to within ±10% of final values. In Fig. 9, the results of analyzing data sets containing 20,000 single laser shots in the spray flame are shown. The lines shown in Fig. 9 represent the cumulative average of the temperature determined from the data shots preceding the given laser shot. On average, the temperature measured at each point converged to within ±3.3% of its mean value within 400 ms (2,000 laser shots). The dashed vertical line represents the length of a typical data acquisition at most data points during radial scans (2,300). This is sufficiently long to collect adequate statistics given that the eddy turnover time for an integral length scale is approximately 1 ms.

4.2. Spectral Fitting Profiles

Thermometry measurements using CPP fs CARS were made at the discrete probe volume locations to spatially resolve thermal gradients in these spray flames. Smooth spatial profiles were produced using bilinear interpolation between discrete measurement locations with information on spatial trends in the temperature field as well as in measurement performance. The panels in Fig. 10 show, from left to right, the mean measured temperature, its standard deviation, and average fitting error. The two-dimensional contour plots should be interpreted with some caution given that they were constructed from a fairly coarse vertical grid of measurement locations.

The average temperature map shows a smoothly-varying axial profile above the pilot from near 2,500 K into the spray flame region. The peak radial temperature for any axial location never drops below 2,000 K indicating this dilute spray flame is well anchored to the pilot. The high-

temperature region is clearly expanding in the radial direction with height as the reaction zone grows. The temperature standard deviation profile builds on the information from the average data adding a relative measure of time-dependence. Finally, the 2-D profile of fitting error yields spatial uncertainty information on the predicted temperatures.

Uncertainty in the accuracy of the CPP fs CARS technique depends on temperature and this was characterized to be 11.3% at room temperature and 2.8% on average at flame temperatures, as described in Section 2.5. Additionally, the fitting error profile interpolated from a set of experimental radial scans describes the spectral fitting performed for the specific data set in question. Temperature data acquired along the radial locations of r/D = ±0.6, for example, have a higher degree of uncertainty than those obtained along the radial locations at r/D = ±1.0. This trend is in contrast to that observed in the calibration flames. Fitting error is typically worse at higher temperatures due to lower signal-to-noise ratio. We attribute this anomaly in the fitting error profile to the unpredictability of the non-resonant background in regions where the chemical composition fluctuates. Single-shot spectral fitting of data obtained in the Hencken burner flame does not exhibit strong fluctuations in the ratio of resonant to non-resonant molecular response at any temperature. This region of higher fitting error is not due to turbulent temperature fluctuations alone, as each single CARS signal spectrum is fit independently.

4.3. Average Temperature Profiles vs Spray Density

One of the novel features of SYNSBURN^{TM} apparatus is the ability to adjust the recess length between the burner orifice and the tip of the liquid injection needle. This allows direct control of the spray density without altering fuel loading or airblast velocity. Fig. 11 shows the average temperature profiles for a single acetone spray flame with the same air and fuel flow rates, but with decreasing needle recess length.

Increasing the recess length enhances spray homogeneity, and this effect is dependent on the residence time of the fuel spray in the main airblast jet. The axial temperature profile for recess length, Lr=80 mm shows a smooth decrease from the peak pilot temperature, and never drops below 1,800 K suggesting the spray is igniting and anchored effectively at Lr = 80 mm. This was

not the case, however, for the spray of highest density, N-AF2-00. This flame case has zero recess length (Lr = 0), so the liquid fuel has essentially no time to atomize in the airblast jet. The axial temperature profile in the rightmost panel decreases to nearly room temperature above the pilot on the left side. At Lr= 0, the spray is fully dense, and the pilot does not appear to effectively anchor the flame. Liquid fuel accumulated in the exhaust hood during testing of these dense spray flames suggesting that the overall combustion efficiency is very low for this case. There is a clear trend in the peak temperature profiles of the two intermediate cases, N-AF2-10 and N-AF2-25 indicating lower heat release with increasing spray density. The peak temperatures in the Lr=25mm case decrease below 1,500 K, but then increase downstream of x/D=10 back above 1,750 K. This suggests the spray flame was anchored, but that droplet evaporation was probably slow compared to the axial velocity.

4.4. Histograms for Modal Analysis of Single-Shot Data

Average temperature profiles and histograms of the corresponding temperature distributions in all spray flames are similar across radial scans at the lowest axial positions of x/D = 0.4 and 1.0. Radial scans at these heights are essentially measuring the pilot flame with profile shapes most closely resembling the 'top hat' shape. Histograms show temperature distributions that are relatively Gaussian except near the interface between the jet and pilot flame at r = 6 mm. The 'M' shape from the 'top hat' profile spreads with height as the flame broadens. The temperature distributions broaden rapidly at the inner radius of the pilot flame r/D = 0.6 at axial position of three diameters above the jet exit where fuel droplets are likely to interact with the high-temperature pilot gases. In several of the histograms shown in Fig. 12, there is a spike at the temperature of the lower search limit of the fitting process, 200 K. The fitting errors on these spectra are still within acceptable bounds, so these are definitely low temperature spectra, but of course not as low as 200 K.

Fig. 12 displays the temperature distribution in corresponding histograms for all radial scans performed in an acetone spray flame of moderate spray density (N-AF2-40). Temperatures are normally distributed across the radial profiles up to x/D=3, above which the distributions

develop more skew toward lower temperature. At radii outside the pilot flame, the temperature distributions also develop slight bimodality at axial locations above x/D=5.

4.5. Fourier Analysis of the Temperature Fields

The 5 kHz data rate can support Fourier analysis up to 2,500 Hz according to the Nyquist criterion of sampling at twice the highest frequency analyzed. With the time sequenced temperature measurements of ~2,000 points in length and 50% overlap used in segmenting windows, the spectral resolution in this Fourier analysis is approximately 9.8 Hz, and the most significant features are resolved. Increasing the length of the time sequence to ~20,000 points, the spectral resolution decreases to 0.6 Hz and weaker features become apparent as shown in Fig. 13.

The periodic peaks visible in the high-resolution panel in Fig. 13 show weak but distinct features at multiples of 454.7 Hz which were present in other spray flames at x/D = 10. The purity of this feature and its harmonics suggests an acoustic source, such as a Helmholtz resonator or possibly a pipe resonator on the order of 10 cm in length of which several potential candidates exist in the SYNSBURN^{TM} gas feed system. Pressure waves from such an oscillation could potentially drive variations in heat release forming a thermoacoustic coupling with the spray flame.

Gradients in the average temperature profiles and the corresponding temperature distribution histograms revealed the inner and outer radii above the pilot flame as regions of interest due to their susceptibility to hydrodynamic instabilities. The temperature spectrum in this shear layer shows the development of an instability near 150 Hz starting at x/D = 1, growing through x/D = 5 before decreasing further downstream. All spray flames exhibit this temperature oscillation at approximately 150 Hz in the shear layer between the flame zone and co-flow. Given that these structures seem to dissipate by x/D = 10, they are most likely due to shear layer instabilities.

These structures dissipate with downstream distance, suggesting that these instabilities are probably not strongly coupled with or amplified by heat release in the spray flames. Farther downstream, broadband, low-frequency temperature fluctuations develop near centerline. Fig. 14 shows the full radial power spectral density (PSD) profiles for two flames cases: N-AF2-40 (left column of panels) and N-AF8-80 (right column of panels). The buildup and decay of the

150-Hz temperature instabilities is evident in both flames. Total temperature fluctuation levels were higher for the N-AF2-40 case than for the N-AF8-80 case. In a non-reacting case with the same flow rates, lower turbulence levels would be expected for N-AF2, as the jet velocity is approximately 30% lower. The observed trend in the PSD radial profiles with height indicates a difference in the flame structure between these two cases due either to increased fuel loading or increased spray density.

5. Conclusions

This work documents the first CPP fs CARS measurements in a spray flame and highlights the processes used to account for signal interferences and minimize error. Ideal system performance was measured using a nearly-adiabatic H_2-air flame stabilized over a Hencken burner typically twice on each testing day. The averages from the 17 different sets of calibrations yielded temperature measurement performance in terms of the uncertainty in the accuracy (absolute) and the single–shot measurement precision ranging from 11.3% and ±5.8 at room temperature to 2.8% and ±3.4 on average at flame temperature. The maximum systematic uncertainty in the flame temperature measurements is estimated to be ±7%. These uncertainties in accuracy (absolute) and precision results are valid for CPP fs CARS single-shot temperature measurements performed in the spray flame in regions with minimal droplet interference, specifically away from the centerline where fuel spray density is highest.

Two distinct types of interference from fuel droplets near the probe volume were observed and attributed to the passage of liquid and vapor fuel through the probe volume. The first effect resulted in strong broadband emission that typically resulted in camera saturation from liquid droplets passing through the probe volume. This phenomenon was attributed to non-linear optical effects of the intense laser pulses in the liquid fuel droplets at the probe volume. Although this phenomenon resulted in camera saturation and loss of data, the affected spectra were easily rejected based on fitting error. The second type of interference produced resonant signal in the high-frequency region of the vibrational nitrogen CARS signal due to passage of presumably gas-phase hydrocarbons through the probe volume. This second type of interference was more nefarious in that the shape of the CPP fs CARS spectrum was only slightly modified. The single-shot fitting code frequently compensated for the altered spectral shape

converging on temperatures that are too high without triggering the error threshold. The temperature error due to the interference from fuel vapor in the probe volume was directly observed at the exit plane on centerline. The average temperatures measured were generally slightly higher than the two neighboring points in the radial dimension even though those points were closer to the high-temperature pilot flame. A possible solution to this problem that we are currently investigating is to apply moderate chirp to both the pump and Stokes beams so as to excite the vibrational nitrogen resonance more selectively [32]. This has the additional advantage of decreasing the influence of the nonresonant background on the CPP fs CARS signal by spectral narrowing of the nonresonant signal.

As evident from examining the temperature histories, fluctuations are well-resolved over most of the flame regions measured. Temperature histories may not be temporally resolved at some positions above ten diameters in height, and specifically along the inner radius of the pilot flame where the spray induction zone is expected. However, the 5-kHz data rate is probably within an order of magnitude of that required to fully resolve temperature fluctuations since most of the flame region does appear temporally resolved.

Despite the harsh environment presented by a turbulent piloted spray burner (SYNSBURN^{TM}), the CPP fs CARS system was used to perform reliable temperature measurements over the region of interest at 5 kHz for several flame cases of various spray density, fuel loading, and with two different types of fuel. The success of CPP fs CARS in spray flames is attributed to the short temporal duration (nanosecond pulses have this advantage as well) and small probe volume size that result in excellent spatial and temporal resolution. The probability of a fuel droplet passing through the probe volume during the approximately 2-ps CARS event is relatively low. Although increasing the laser PRF beyond 5 kHz and employing more advanced spectral fitting algorithms would improve the technique, CPP fs CARS thermometry appears to be well-suited for thermometry in turbulent spray flames.

Funding Information: Funding for this research program was provided by the U.S. Department of Energy, Division of Chemical Sciences, Geosciences and Biosciences, Grant No. (DE-FG02-03ER15391) and by the King Abdullah University of Science and Technology, CCF subaward (No. 1975-01).

Acknowledgment: During this period of effort, Levi Thomas was a PhD candidate in the Department of Mechanical Engineering at Purdue University and supported by a fellowship from the Purdue Military Research Initiative. The University of Sydney Combustion Group is funded by the Australian Research Council. Grant # : ARC-DP180104190.

References:

[1] S. Blakely, L. Rye, C.W. Wilson, Aviation gas turbine alternative fuels: A review, Proc. Combust. Inst. 33 (2), 2863-2885 (2011).
[2] C. Schulz, V. Sick, Tracer-LIF diagnostics: quantitative measurement of fuel concentration, temperature and fuel/air ratio in practical combustion systems, Prog. Energy Combust. Sci. 31 (1), 75-121 (2005).
[3] C. Noehre, M. Andersson, B. Johansson, A. Hultqvist, Characterization of partially premixed combustion, SAE Technical Paper 2006-01-3412, (2006).
[4] A.C. Eckbreth, Laser Diagnostics for Combustion Temperature and Species, Taylor & Francis Group, 1996.
[5] S.H. Starner, J. Gounder, A.R. Masri, Effects of turbulence and carrier fluid on simple, turbulent spray jet flames, Combust. Flame, 143 (4), 420-432 (2005).
[6] J.A. Friedman, M. Renksizbulut, Investigating a methanol spray flame interacting with an annular air jet using phase-Doppler interferometry and planar laser-induced fluorescence, Combust. Flame 117 (1999).
[7] J. Gao, D.R. Guildenbecher, P.L. Reu, V. Kulkarni, P.E. Sojka, J. Chen, Quantitative, three-dimensional diagnostics of multiphase drop fragmentation via digital in-line holography, Opt. Lett. 38 (11), 1893-1895 (2013).
[8] A. Lowe, A. Kourmatzis, A.R. Masri, Turbulent spray flames of intermediate density: Stability and near field structure, Combust. Flame, vol. 176, pp. 511–520, Feb. 2017.
[9] G. Grunefeld, V. Beushausen, P. Andresen, W. Hentschel, Spatially resolved Raman scattering for multi-species and temperature analysis in technically applied combustion systems: Spray flame and four-cylinder in-line engine, Appl. Phys. B 58 (4), 333-342 (1994).
[10] A.M. Mellor, Gas turbine engine pollution, Prog. Energy Combust. Sci. 1, 111-133 (1976).
[11] C.J. Kliewer, Y. Gao, T. Seeger, J. Kiefer, B.D. Patterson, T.B. Settersten, Picosecond time-resolved pure-rotational coherent anti-Stokes Raman spectroscopy in sooting flames, Proc. Comb. Inst. 33 (2011).
[12] S.P. Kearney, K. Frederickson, T.W. Grasser, Dual-pump coherent anti-Stokes Raman scattering thermometry in a sooting turbulent pool fire, Proc. Combust. Inst. 31 (1), 871-878 (2009).
[13] F. Beyrau, M.C. Weikl, I. Schmitz, T. Seeger, A. Leipertz, Locally resolved investigation of the vaporization of GDI sprays applying different laser techniques, Atomization and Sprays 16 (3), 319-330 (2006).
[14] A Satija, R.P. Lucht, Development of a combined pure rotational and vibrational coherent anti-Stokes Raman scattering system, Optics Lett. 38 (8), 1340-1342 (2013).
[15] J.R. Gord, T.R. Meyer, S. Roy, Applications of ultrafast lasers for optical measurement in combusting flows, Annual Rev. Anal. Chem. 1 (2008).
[16] C.N. Dennis, C.D. Slabaugh, I.G. Boxx, W. Meier, R.P. Lucht, Chirped probe pulse femtosecond coherent anti-Stokes Raman scattering thermometry at 5 kHz in a gas turbine model combustor, Proc. Combust. Inst. 35 (3), 3731-3738 (2015).
[17] C.N. Dennis, A. Satija, R.P. Lucht, High dynamic range thermometry at 5 kHz in hydrogen–air diffusion flame using chirped-probe-pulse femtosecond coherent anti-stokes Raman scattering, J. Raman Spect. 47, 177-188, (2015).
[18] C.N. Dennis, C.D. Slabaugh I. Boxx, W. Meier, R.P. Lucht, 5 kHz thermometry in a swirl-stabilized gas turbine model combustor using chirped probe pulse femtosecond CARS. Part 1: Temporally resolved swirl-flame thermometry, Combust. Flame 173 (2016).

[19] C.D. Slabaugh, C.N. Dennis, I. Boxx, W. Meier, R.P. Lucht, 5 kHz thermometry in a swirl-stabilized gas turbine model combustor using chirped probe pulse femtosecond CARS. Part 2. Analysis of swirl flame dynamics, Combust. Flame 173 (2016).
[20] F. Beyrau, A. Brauer, T. Seeger, A. Leipertz, Gas-phase temperature measurement in the vaporizing spray of a gasoline direct-injection injector by use of pure rotational coherent anti-Stokes Raman scattering, Optics Letters 29 (2004).
[21] S.R. Engel, A.F. Koegler, Y.Gao, D. Kilian, M. Voigt, T. Seeger, W. Peukert, A. Leipertz, Gas phase temperature measurements in the liquid and particle regime of a flame spray pyrolysis process using O2-based pure rotational coherent anti-Stokes Raman scattering, Appl. Opt. 51 (2012).
[22] A. Lowe, L.M. Thomas, A. Satija, R.P. Lucht, and A.R. Masri, Chirped-probe-pulse femtosecond CARS thermometry in turbulent spray flames, Proc. Combust. Inst. 37 (2018), https://doi.org/10.1016/j.proci.2018.06.149.
[23] A. Lowe, L.M. Thomas, A. Satija, R.P. Lucht, and A.R. Masri, Five kHz Thermometry in Turbulent Spray Flames using Chirped-Probe- Pulse Femtosecond CARS, Part II: Structure of Reaction Zones, Combust. Flame (2018), https://doi.org/10.1016/j.combustflame.2018.10.22.
[24] L.M. Thomas, A. Satija, R.P. Lucht, Technique developments and performance analysis of chirped-probe-pulse femtosecond coherent anti-Stokes Raman scattering combustion thermometry, Appl. Opt. 56, 8797-8810 (2017).
[25] J.D. Miller, C.E. Dedic, S. Roy, J.R. Gord, T.R. Meyer, Interference-free gas-phase thermometry at elevated pressure using hybrid femtosecond/picosecond rotational coherent anti-Stokes Raman scattering, Optics Express 20 (2012).
[26] T. Lang and M. Motzkus, Single-shot femtosecond coherent anti-Stokes Raman-scattering thermometry, J. Opt. Soc. Am. B 19 (2002) 340-344.
[27] S. Roy, W.D. Kulatilaka, D.R. Richardson, R.P. Lucht, J.R. Gord, Gas-phase single-shot thermometry at 1 kHz using fs-CARS spectroscopy, Opt. Lett. 34 (2009) 3857-3859.
[28] R.P. Lucht, P.J. Kinnius, S. Roy, J.R. Gord, Theory of femtosecond coherent anti-Stokes Raman scattering spectroscopy of gas-phase transitions, J. Chem. Phys. 127 (2007).
[29] D.R. Richardson, R.P. Lucht, W.D. Kulatilaka, S. Roy, J.R. Gord, Theoretical modeling of single-laser-shot, chirped-probe-pulse femtosecond coherent anti-Stokes Raman scattering thermometry, Appl. Phys. B 104 (2011).
[30] T.F. Guiberti, H.Cutcher, W.L. Roberts, A.R. Masri, Influence of pilot flame parameters on the stability of turbulent jet flames, Energy and Fuels 31 (2017) 2128–2137.
[31] T. Yamaji, T. Saito, K. Hayamizu, M. Yanagisawa, O.Yamamoto, Spectral Database for Organic Compounds: acetone and ethyl alcohol Information pages, National Institute of Advanced Industrial Science and Technology, < http://sdbs.db.aist.go.jp> Accessed June2017.
[32] M. Gu, A. Satija, and R.P. Lucht, “Effects Of Moderate Pump and Stokes Chirp on Chirped-Probe Pulse Femtosecond Coherent Anti-Stokes Raman Scattering Thermometry,” Paper AIAA-2018-1024, presented at the 2018 AIAA SciTech Meeting, Kissimmee, Florida, 8-12 January 2018.

Figures:

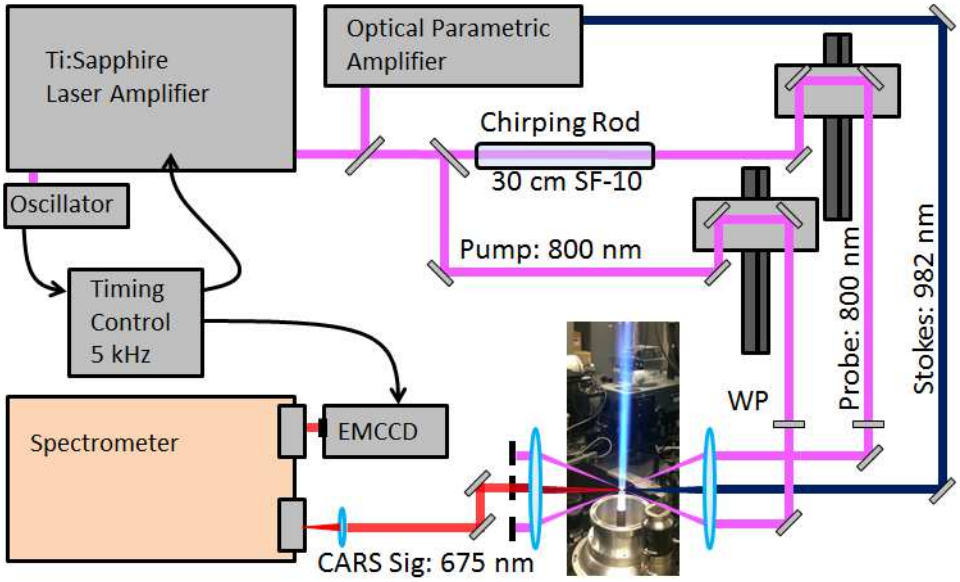

Fig. 1. Diagram of the CPP fs CARS experimental system with picture of an ethanol spray flame above the SYNSBURN mounted in a co-flow wind tunnel apparatus.

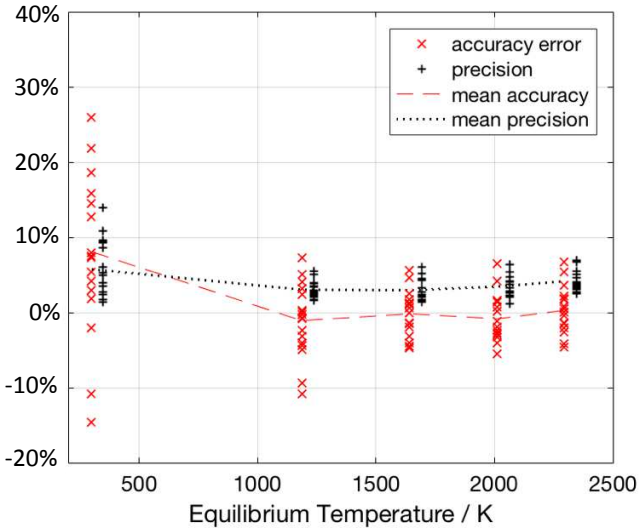

Fig. 2. Aggregated temperature measurement performance test results from Hencken burner calibration measurements during testing of all spray flames. Red 'x' and black '+' symbols display accuracy and precision respectively.

Table 1. Performance averages during spray-flame measurements

Eqv. Ratio ϕ =	CPP fs CARS SS Performance			
	T_{ad} (K)	Accuracy (abs.)	Avg. Accuracy (Mean Temp. Bias)	Precision (±1 σ)
0.0	295	11.3%	8.1%	±5.8%
0.3	1187	3.7%	-1.1%	±3%
0.5	1641	2.3%	-0.2%	±3%
0.7	2012	2.7%	-0.8%	±3.4%
0.9	2295	2.4%	0.3%	±4.2%
Avg. of Flame Cases:		2.8%	-0.4%	±3.4%

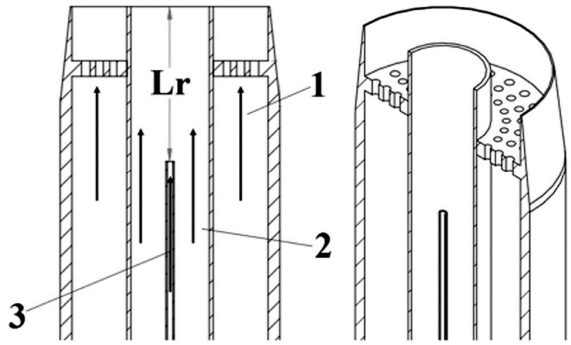

Fig. 3. Cross-section schematic diagram of SYNSBURN (left) and isometric view (right) showing three fluid paths: (1) the pilot stream with 25-mm outer diameter, (2) the main air jet stream with 10-mm diameter, and (3) liquid fuel stream with a 686-μm needle diameter. Used with permission from [8].

Table 2. Initial flow rate conditions for the acetone (A) and ethanol (E) spray flame cases

Cases	N-AF2	N-AF6	N-AF7	N-AF8
U_j(m/s)	36	36	60	48
Re_g	21281	21281	35468	28374
Q (g/min)	75	45	75	45
Re_l	6967	4180	6967	4180
We	45	45	126	80
F/A (by mass)	0.37	0.22	0.22	0.17

Cases	N-EF2	N-EF6	N-EF7	N-EF8
U_j(m/s)	36	36	60	48
Re_g	21281	21281	35468	28374
Q (g/min)	75	45	75	45
Re_l	19496	11698	19496	11698
We	48	48	135	86
F/A (by mass)	0.37	0.22	0.22	0.17

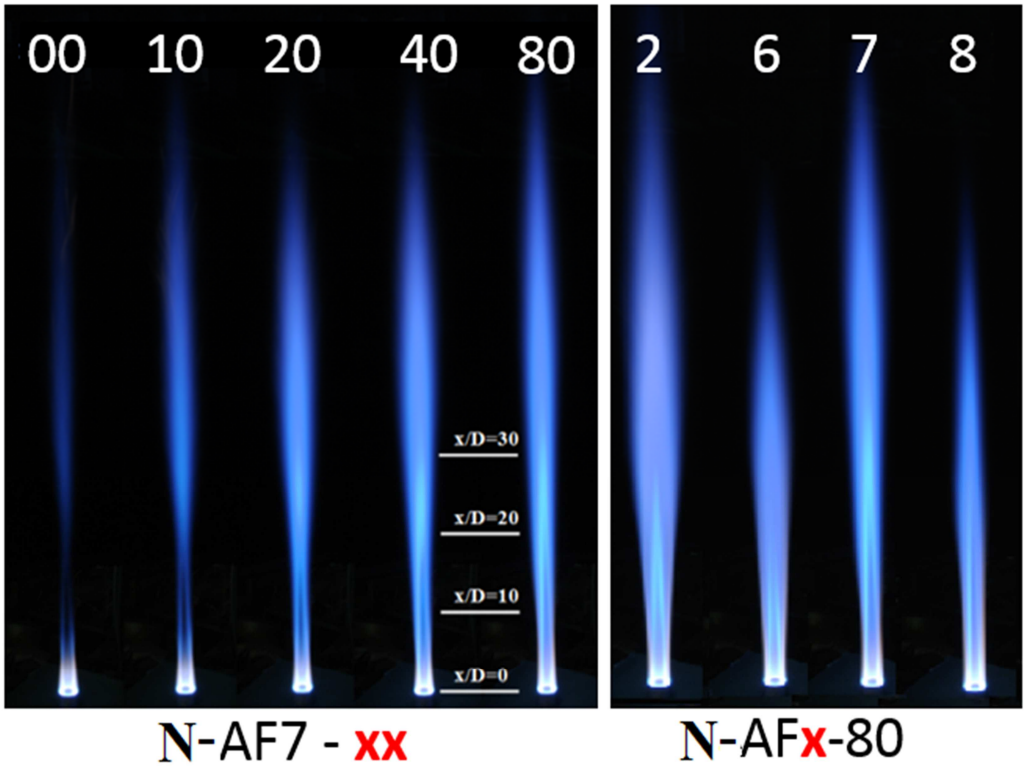

Fig. 4. Long-exposure (1s) pictures of acetone spray flames. Left: N-AF7 with needle recess length 'xx' ranging left to right from 0 to 80 mm. Right: Spray flame cases for fixed 80mm needle recess length but varying initial flow conditions. Images modified with permission from [8].

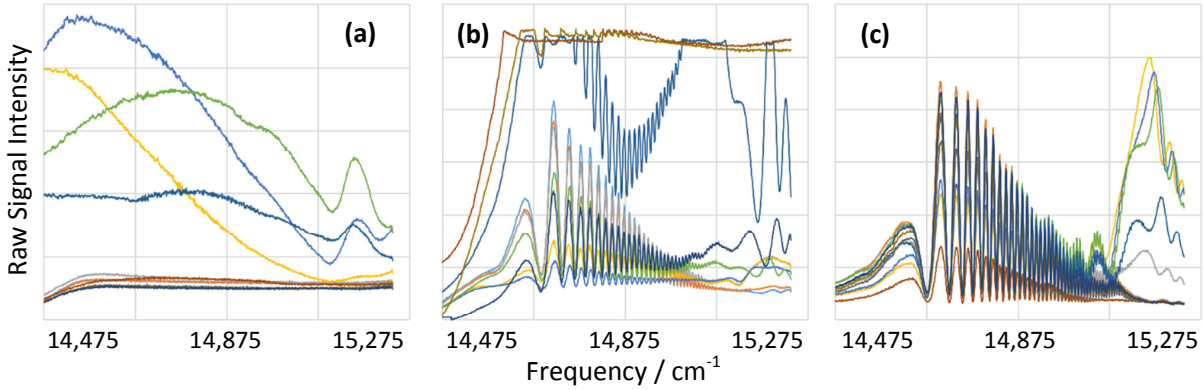

Fig. 5. Selected sequences of 10 laser shots are overlaid in each plot showing interference during passage of fuel through the probe volume. Sequence in panel (a): the Stokes beam is blocked, and the spectra show interference from liquid droplets. Sequence in panel (b) measured at the exit plane in a dense spray: N-AF2-40. Interferences from both liquid and gas-phase hydrocarbons are evident. Sequence in panel (c): measured at downstream position (x/D=20) in dilute spray: N-AF8-80. Interferences from only gas-phase hydrocarbons evident.

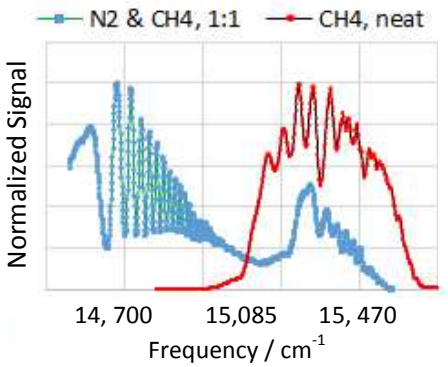

Fig. 6. Time-averaged, and normalized CPP fs CARS signals measured in a gas cell at room temperature. Green line with blue squares shows equal parts N_2 & CH_4 with the laser system tuned directly to N_2 vibrational resonance; the increase in signal level around 15,300 cm^{-1} is from the CH_4. Black line with red circles shows pure methane with laser system tuned directly to a CH_4 vibrational resonance (ν_1).

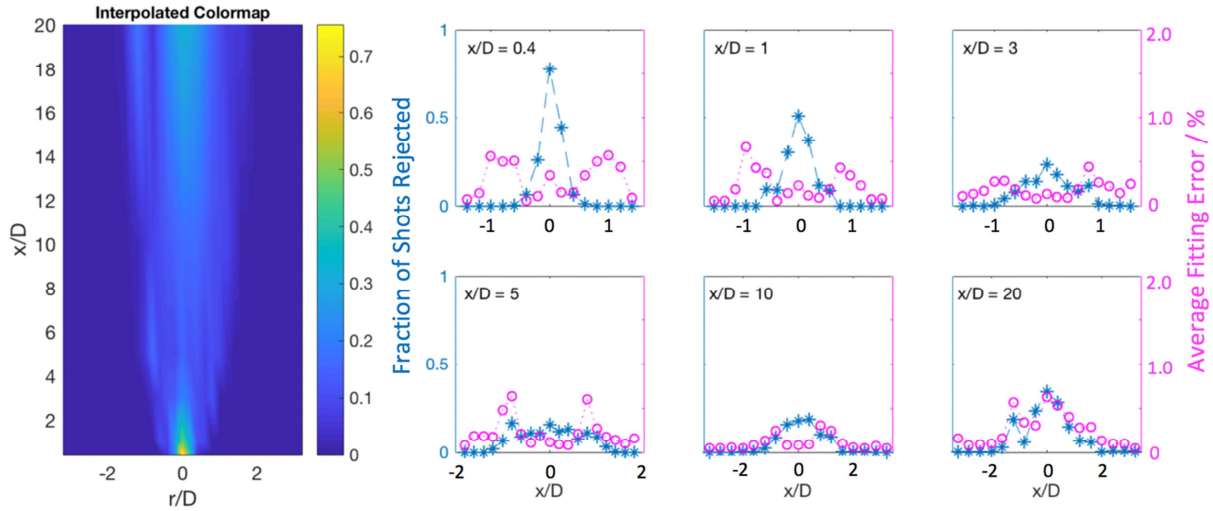

Fig. 7. Single shot rejection profiles for the N-AF2-40 acetone flame measured at heights x/D = [0.4 1.0 3.0 5.0 10 20]. Interpolated colormap showing spatial profile (left). Corresponding radial profiles (right) with the fraction of shots rejected on the left ordinate (star symbols) and the average fitting error (circle symbols) on the right ordinate. The average fitting error was calculated after excluding rejected shots above the threshold of 2%.

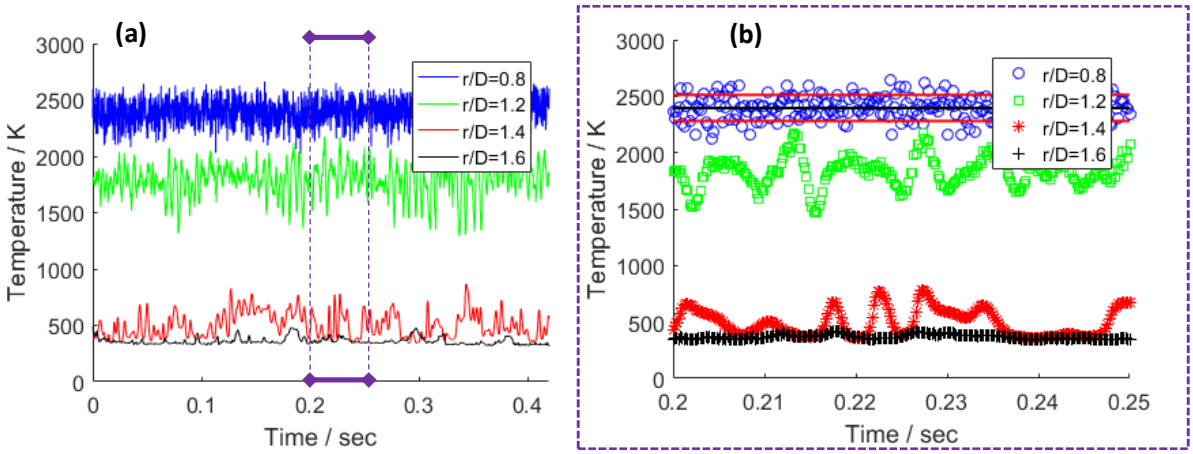

Fig. 8. Temperature history at x/D=1 in an acetone spray flame (N-AF2-40) for several radial positions. (**a**): full time history of over two thousand shots. (**b**) zoom view of 50 ms showing 250 shots. Solid black and red lines in panel (b) show temperature average (2396 K) and RMS values (±4.83%).

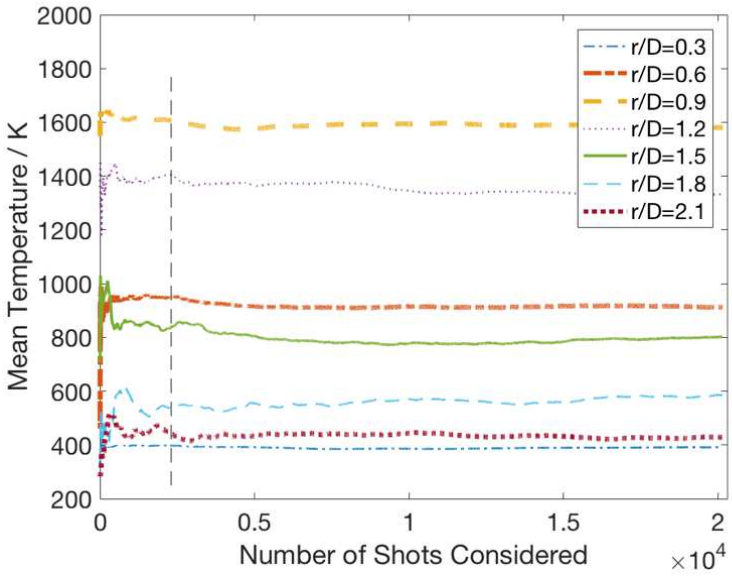

Fig. 9. Temperature convergence of dilute acetone spray flame, N-AF8-80, at axial position x/D = 10.

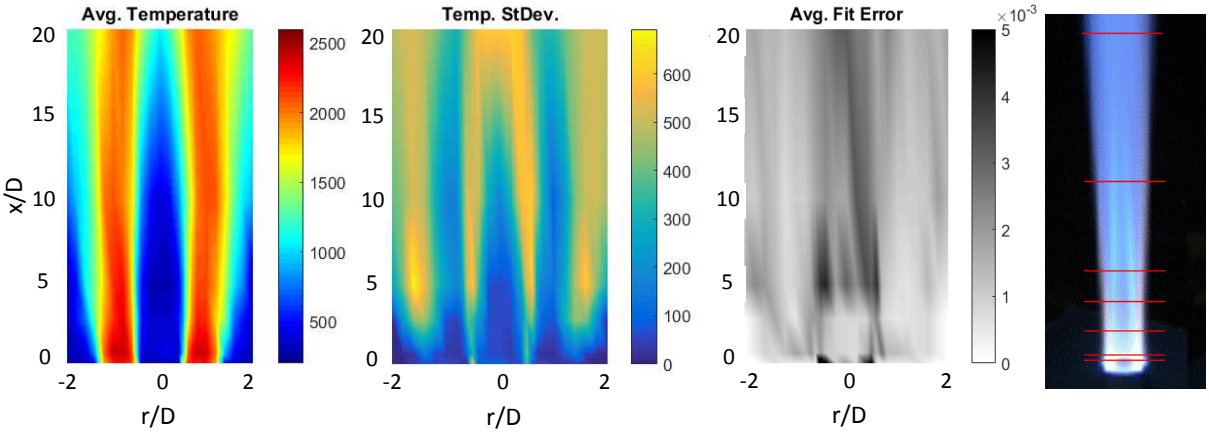

Fig. 10. Interpolated average profiles resulting from full radial scan of one flame case, N-AF6-80 ($\dot{Q}_{max}$ = 22 kW). From left to right, 2-D color-map panels show profiles of average temperature in deg K, the temperature standard deviation in deg K, and the average squared fitting error. The radial scale is expanded for detail, but the height and radial scales are common among the color maps for direct comparison. Red lines in the flame image (far right) show the approximate locations of radial scans.

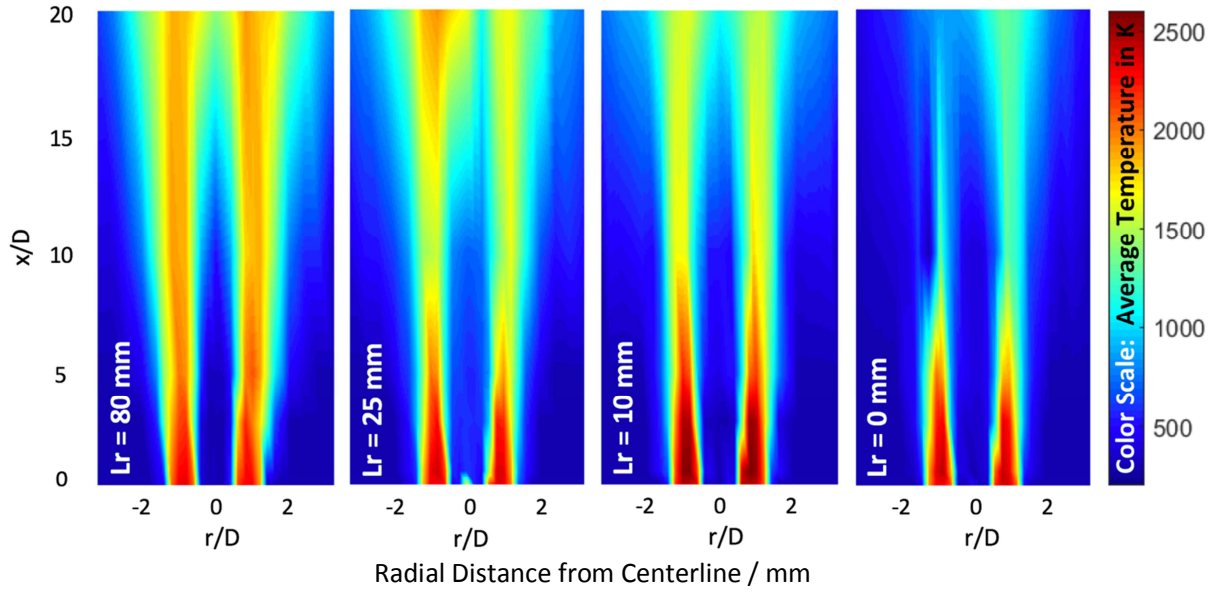

Fig. 11. Average temperature profiles interpolated from full radial scans of the same acetone spray flame, N-AF2 ($\dot{Q}_{max}$ = 36 kW), at four different needle-recess lengths, Lr = 80, 25, 10, and 0 mm.

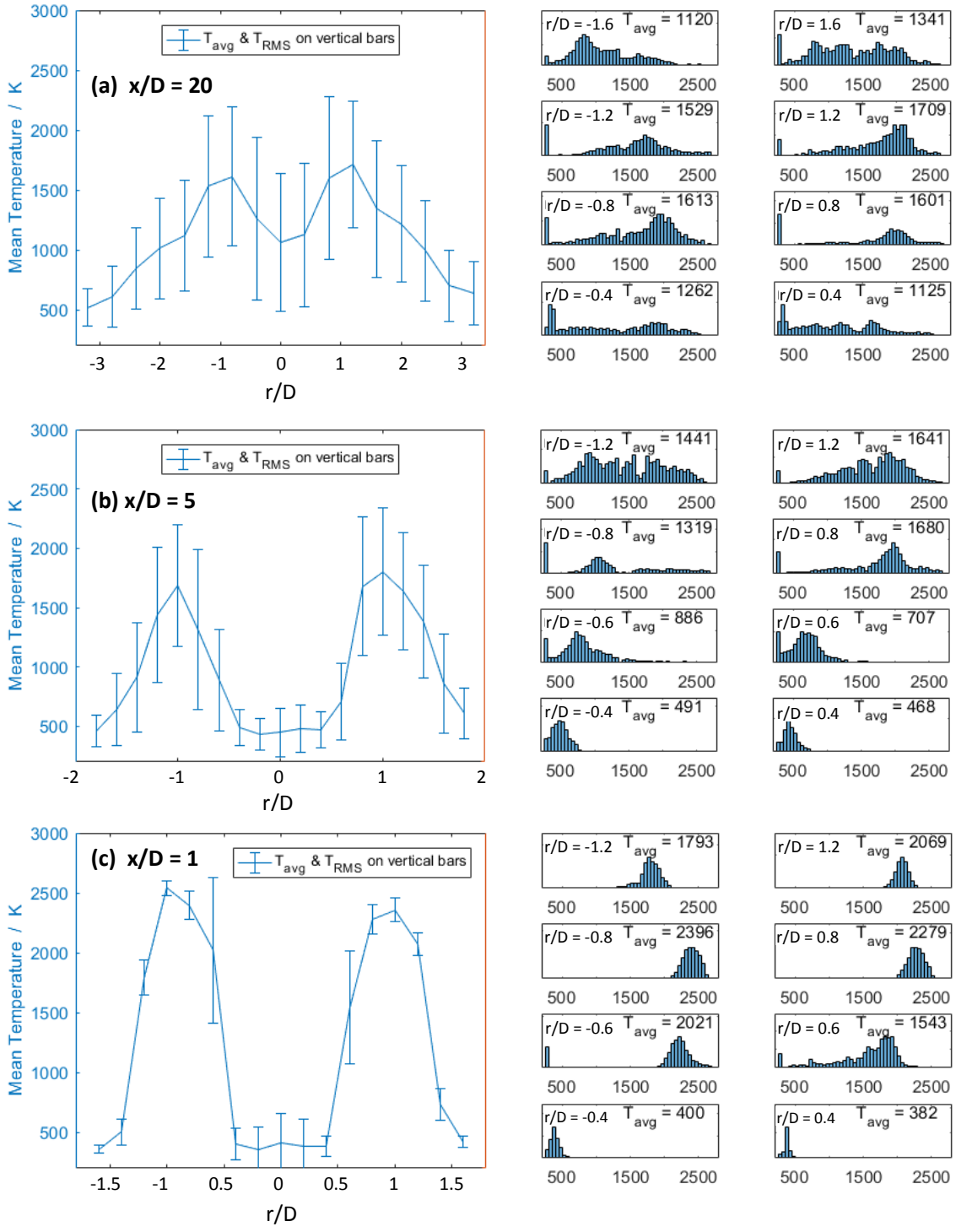

Fig. 12. Average temperature profiles from radial scans performed at x/D= 20 (a), 5 (b), & 1.0 (c) in an acetone spray flame (N-AF2-40) with accompanying histograms shown in right subpanels. Left panels: average temperature profile in blue with standard deviation error bars.

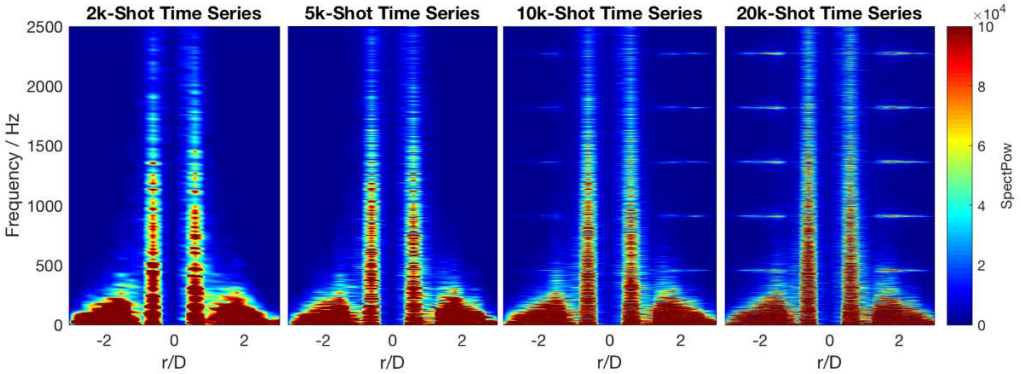

Fig. 13. Power spectral density convergence of N-AF2-80 radial profile at x/D = 10.

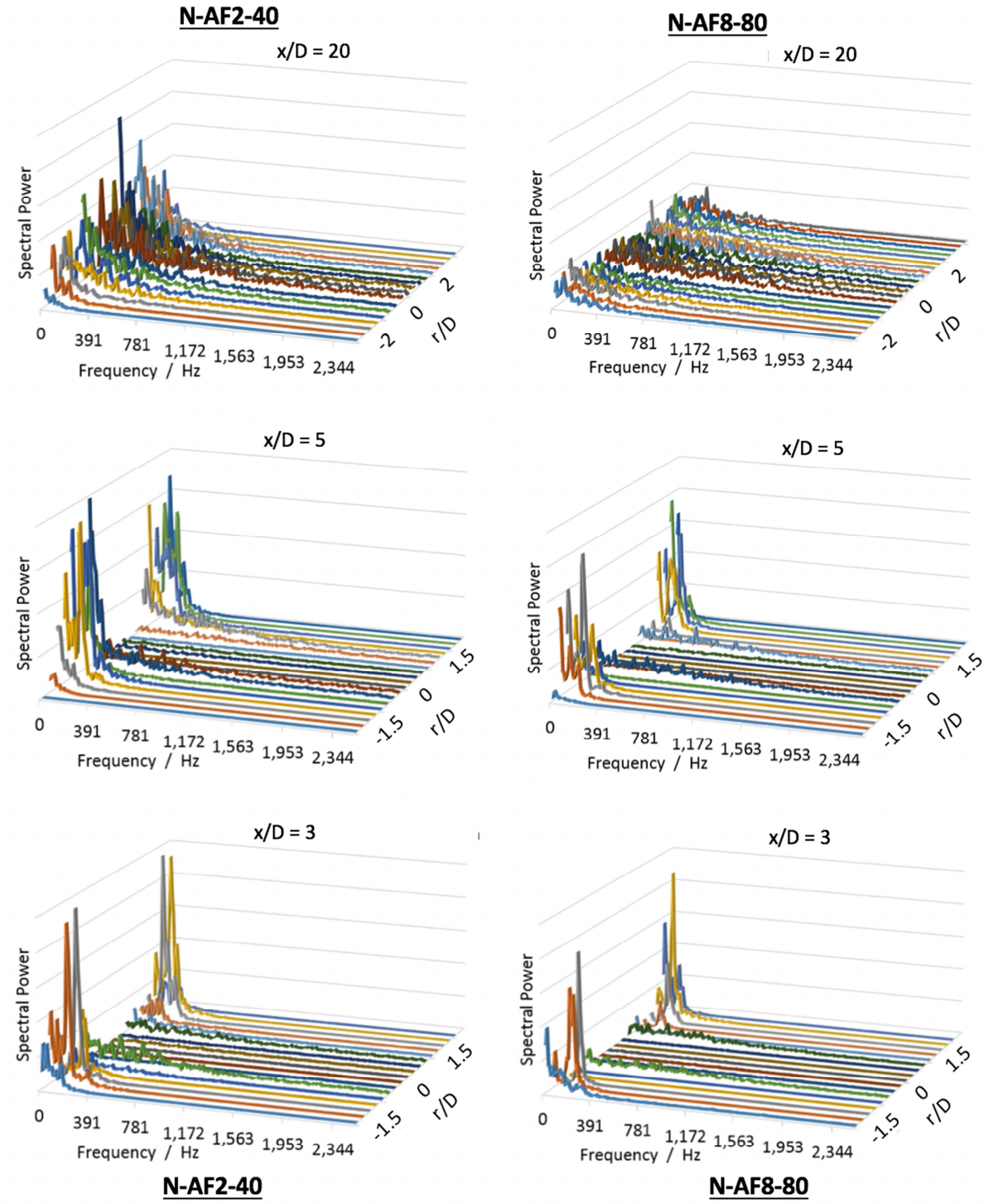

Fig. 14. Full PSD radial profiles for two acetone spray flames at axial locations x/D = [3.0 5.0 20]. Left column of panels corresponds to N-AF2-40 (moderate density spray and higher fuel loading); right column of panels corresponds to N-AF8-80 (dilute spray at lower fuel loading). Spectral power has been normalized in all panels for comparison by the highest measured value of spectral power: 2E6 K^2/Hz.